


Influence of the Atlantic meridional overturning circulation on the U.S. extreme cold weather

Jianjun Yin ¹✉ & Ming Zhao²

Due to its large northward heat transport, the Atlantic meridional overturning circulation influences both weather and climate at the mid-latitude Northern Hemisphere. Here we use a state-of-the-art global weather/climate modeling system with high resolution (GFDL CM4C192) to quantify this influence focusing on the U.S. extreme cold weather during winter. We perform a control simulation and the water-hosing experiment to obtain two climate states with and without a vigorous Atlantic meridional overturning circulation. We find that in the control simulation with an overturning circulation, the U.S. east of the Rockies is a region characterized by intense north-south heat exchange in the atmosphere during winter. Without the northward heat transport by the overturning circulation in the hosing experiment, this channel of atmospheric heat exchange becomes even more active through the Bjerknes compensation mechanism. Over the U.S., extreme cold weather intensifies disproportionately compared with the mean climate response after the shutdown of the overturning circulation. Our results suggest that an active overturning circulation in the present-day climate likely makes the U.S. winter less harsh and extreme.

¹Department of Geosciences, University of Arizona, Tucson, USA. ²NOAA/GFDL, Princeton, USA. ✉email: yin@arizona.edu

The important role of the Atlantic Meridional Overturning Circulation (AMOC) in the climate system has been extensively studied^{1–12}. Without an AMOC and associated northward heat transport, northern and western Europe could be much colder^{1,2,5,6,9}, the Arctic sea ice could expand¹, the Inter-Tropical Convergence Zone (ITCZ) could shift southward^{3,5,9}, and sea level along the East Coast of North America could be higher¹². Compared with these changes in the mean climate, the impact of AMOC on extreme weather has not been investigated systematically and sufficiently thus far. One reason is that previous generations of global climate model were particularly designed for studies on large-scale, long-term climate, rather than on daily weather at the local scale, which requires high resolution, frequent data output, regional focus, and so on. Nonetheless, several recent studies have shown that a slowdown of AMOC could contribute to summer heatwaves over Europe^{13,14}, flooding and droughts¹⁵, stronger and more active Atlantic hurricanes^{16,17} and extratropical storms¹⁸.

During the past decade, the Geophysical Fluid Dynamics Laboratory (GFDL) of NOAA has been working towards a unified and seamless modeling system suitable for studying both weather and climate, as well as their complex interactions under the same umbrella. The recent progress in model development and the rapid growth of supercomputer power have provided better tools to tackle important weather-climate issues. Here, we use the high resolution version (C192) of the global coupled modeling system, GFDL CM4^{19–23} (see the “Methods” section), to investigate the influence of AMOC on the U.S. extreme cold weather during winter. As low-frequency high-impact events, extreme cold snaps could be disastrous (<https://www.ncdc.noaa.gov/billions/>), particularly for the U.S. southern states with typical mild temperatures during winter^{24,25}.

Results

Control simulation and water-hosing experiment with GFDL CM4C192. Under the 1950 radiative forcing, a long, centennial timescale control simulation has been carried out with CM4C192 as part of the GFDL’s participation in the High Resolution Model Intercomparison Project²⁶. Due to the refined resolution for both the atmosphere (0.5°) and ocean (0.25°), synoptic-scale phenomena are better simulated by CM4C192, including hurricanes and severe winter storms, atmospheric rivers and blocking, ocean eddies and jets, storm surge and coastal flooding, etc^{12,19–21,23}. In addition, the simulated AMOC has a mean strength of about 18 Sv ($1 \text{ Sv} = 10^6 \text{ m}^3 \text{ s}^{-1}$) at 26°N, compared well with observations^{19,23} (Supplementary Fig. 1a).

To investigate the impact of AMOC on mid-latitude weather, we consider an idealized case by obtaining a climate state without an active AMOC while keeping everything else the same. To do so, we perform the typical water-hosing experiment by imposing a 0.6 Sv freshwater addition over the northern North Atlantic^{1,3} (see the “Methods” section for more details). This experimental design should lead to strong and quick signals with a clear and definite attribution to AMOC, thereby avoiding complication by other factors. In addition, the high resolution coupled model is computationally expensive, which currently prevents long, transient, and ensemble simulations.

In response to the freshwater perturbation, the AMOC almost shuts down in about 20 years (Supplementary Fig. 1b, c). The atmosphere in the Northern Hemisphere approaches a new quasi-equilibrium state after year 20. In the following analysis, we compare years 21–100 of the hosing experiment with the 100-year control run to identify response characteristics of daily weather to the AMOC shutdown.

Energy transport across 40°N and Bjerknes compensation between the ocean and atmosphere. In the control run of

CM4C192, the atmosphere and ocean work together to transport up to 5.7 Petawatts (PW, or 10^{15} Watts) annual heat poleward to compensate the differential solar heating between the low and high latitudes^{27–29} (Fig. 1a, b and Supplementary Fig. 2). In the Northern Hemisphere, the maximum total transport occurs at about 40°N. At mid-latitudes, the atmosphere is highly efficient at mixing different temperatures and transporting heat poleward through fast-moving turbulent weather systems, especially during winter. For the annual mean, the oceanic transport of about 0.8 PW at 40°N, largely due to AMOC^{16,30,31}, is by far smaller than its atmospheric counterpart of 4.8 PW, but nonetheless represents an enormous amount of heat in global energy balance (Fig. 1). It should be noted that CM4C192 likely underestimates the northward heat transport in the Atlantic. The simulated maximum transport of about 1 PW at 26°N is lower than the recent observational estimate of about 1.3 PW^{16,31} (Fig. 1c).

We consider the atmosphere north of 40°N as a whole (“northern atmosphere”) and perform a detailed heat budget analysis for December, January, and February (DJF). During boreal winter of the control, the northern atmosphere loses 13.3 PW heat at the top of the atmosphere (TOA) but gains 6.1 PW from the surface (Fig. 1a). The heat deficit of 7.2 PW is compensated by the atmospheric heat transport across 40°N mainly associated with mid-latitude weather processes especially baroclinic transient eddies. Without an AMOC and its northward heat transport in the hosing experiment (Fig. 1c), the TOA and surface heat fluxes reduce by 0.6 PW and 1.1 PW, respectively (Fig. 1a). To compensate the increased heat deficit due to these changes, the atmosphere must transport about 0.5 PW more heat northward across 40°N. This “Bjerknes compensation” mechanism^{32–36} works to stabilize the mean temperature and maintain the energy balance of the northern atmosphere in a climate without AMOC.

The enhanced atmospheric heat transport during winter is achieved through more active weather processes at mid-latitudes³³. In the control, intense north–south atmospheric heat exchanges occur over a broad region at 40°N. At 850 hPa, large atmospheric eddy temperature fluxes²⁷ ($v'T'$; see “Methods” section) are found over the eastern North America and western North Atlantic, East Asia, and the North Pacific, as well as over Europe and Middle East (Fig. 2a). These regions coincide with the mid-latitude storm track where extratropical cyclones and anticyclones continuously develop and propagate, thereby efficiently mixing warm and cold air masses. In particular, the U.S. east of the Rocky Mountains³⁷ sees some of the highest values of $v'T'$ (Fig. 2a).

The atmospheric eddy temperature flux is sensitive to the change in heat transport by AMOC and the surface heat flux anomalies in the northern Atlantic and Arctic (Fig. 2c). After the AMOC shutdown in the hosing experiment of CM4C192, $v'T'$ shows large increases at the northern latitudes (Fig. 2b). North of 40°N, the increase in the eddy sensible heat flux concentrates over the northern North Atlantic, where the mean cooling is largest and amplified due to the sea ice feedback (Supplementary Fig. 3b). South of 40°N, higher $v'T'$ values are pronounced over the eastern U.S. and the North Pacific (Fig. 2b). Note that the southward intrusion of frigid Arctic air mass is equivalent to a large northward temperature flux because both v' and T' are negative and have large absolute values. In addition, the atmospheric eddy latent heat flux ($v'q'$) shows a consistent increase in the 20°–40°N latitudinal band (Supplementary Fig. 4).

Response of the U.S. extreme cold weather to the AMOC shutdown. During years 21–100 in the hosing experiment, the global annual mean surface air temperature cools by about 1 °C

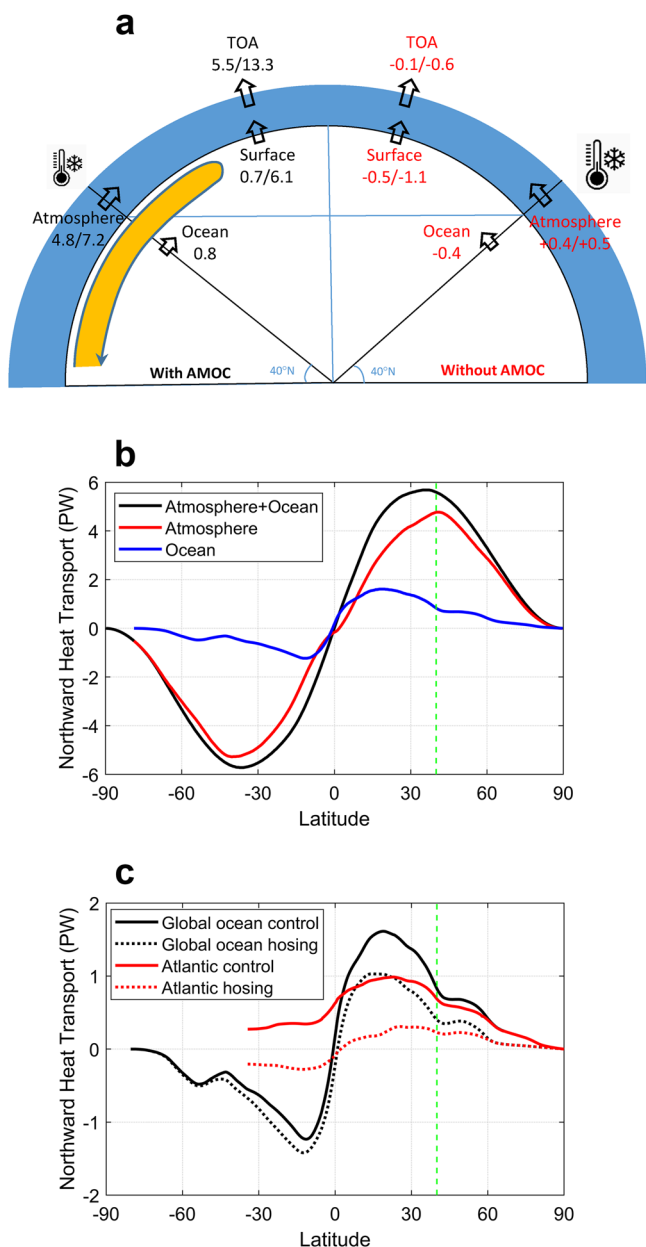


Fig. 1 Energy balance of the northern atmosphere in the climates with and without an active AMOC. **a** Schematic shows the energy balance for the entire atmosphere north of 40°N. The left half with black numbers (annual/DJF) shows heat fluxes (PW) at the top, bottom and southern boundaries in the long-term control run of CM4C192. The right half with red numbers shows the heat flux anomalies during years 21–100 of the hosing experiment relative to the control. The positive and negative values indicate enhanced and reduced heat fluxes, respectively. Only the annual mean value is shown for the oceanic transport. The blue and yellow shadings denote the atmosphere and AMOC, respectively. **b** Annual northward heat transport by the global atmosphere and global ocean as a function of latitude in the control run. **c** Annual northward heat transport of the global ocean and the Atlantic in the control and during years 21–100 of the hosing experiment. The green vertical dashed line marks 40°N.

relative to the control (Supplementary Fig. 5a). This global cooling, centered at the northern North Atlantic, is a result of the cloud, water vapor, and sea ice feedbacks associated with the reduced northward heat transport in the ocean^{38,39}. Other changes of the large-scale mean climate in the hosing experiment are generally similar to the previous results¹.

Next we focus on the U.S. daily surface air temperature (T_s) in DJF. Compared with the reanalysis data of ERA5⁴⁰ during 1979–2021 (see “Methods” section), CM4C192 simulates the mean and daily variations of T_s in DJF well in the control run (Supplementary Fig. 6). As for extremely cold temperatures, we evaluate the model performance at Chicago, Houston, and New York, three large cities representing the Midwest, South, and Northeast U.S., respectively. At Chicago, the daily temperature anomaly relative to the daily climatology (ΔT_s ; see “Methods” section) reached the lowest point of -23.5°C on January 31, 2019 in the detrended and deseasonalized ERA5 data (Fig. 3a, b). The extremeness of the recent Texas cold snap during February 2021 (https://en.wikipedia.org/wiki/February_2021_North_American_cold_wave) is even more striking. ΔT_s at Houston plummeted to -23.4°C on February 16, 2021, by far colder than previous extreme events (Fig. 3c, d). At New York, the coldest ΔT_s occurred on January 18, 1982 and on February 20 and 24, 2015, with a magnitude of about -16.3°C (Fig. 3e, f).

At the three cities, CM4C192 simulates the general statistics of ΔT_s well in the control run, including its standard deviation, skewness, and kurtosis (Fig. 3). However, the model underestimates extreme cold events as evidenced by the higher 10-year and 100-year return levels ($\widehat{\Delta T}_s^{10}$ and $\widehat{\Delta T}_s^{100}$; see “Methods” section for the return level calculation), especially at Houston (Fig. 3). Different resolutions and external forcings, as well as existing model biases, are among the possible reasons for the differences between the ERA5 data and CM4C192 simulations.

After the shutdown of AMOC in the hosing experiment, the intensity and frequency of extremely cold daily temperatures over the U.S. increase disproportionately compared with the mean temperature response (Figs. 4 and 5 and Supplementary Fig. 7). At Chicago, the 10-year and 100-year return levels of $\widehat{\Delta T}_s^{10}$ and $\widehat{\Delta T}_s^{100}$ further drop by 3.4°C and 3.6°C , respectively, in the hosing experiment, compared with a mean cooling of 1.6°C relative to the control (Fig. 4a, b). $\widehat{\Delta T}_s^{100}$ (-20.9°C) in the control is almost identical to $\widehat{\Delta T}_s^{10}$ (-20.8°C) in the hosing run, suggesting that the 100-year extreme cold event could occur every 10 years at Chicago after the AMOC shutdown. At Houston, $\widehat{\Delta T}_s^{100}$ drops more and by 4.6°C from -14.8°C in the control to -19.4°C in the hosing (Fig. 4c, d). It represents a change more than five times larger than the mean cooling of 0.9°C (Fig. 5f). Interestingly, this drop makes $\widehat{\Delta T}_s^{100}$ in CM4C192 closer to that of ERA5 (Fig. 3c, d). At New York, $\widehat{\Delta T}_s^{10}$ and $\widehat{\Delta T}_s^{100}$ further drop by 5.6°C and 5.4°C , respectively, compared with a mean cooling of 2°C (Fig. 4e, f). Extremely cold temperatures reaching or exceeding $\widehat{\Delta T}_s^{100} = -15.7^\circ\text{C}$ in the control occur more frequently and for about 60 times/days in the hosing experiment.

To assess the uncertainty associated with the extreme value analysis, we perform the Kolmogorov–Smirnov test for the annual coldest ΔT_s at Chicago, Houston and New York between the control and hosing runs. The test rejects the null hypothesis at the 5% significance level that the control and hosing samples are drawn from the same distribution. In terms of the return level estimate, we apply the bootstrap method to quantify its 90% confidence bounds⁴¹ (Supplementary Fig. 8). The results confirm that compared with the control, the drops of $\widehat{\Delta T}_s^{10}$ and $\widehat{\Delta T}_s^{100}$ in the hosing experiment are statistically significant at the three cities.

Impact factors for the change in return levels. In the hosing experiment, the drops in return level of extreme cold temperatures could be caused by multiple factors⁴² (Fig. 5): the mean cooling, increased overall variance, reduced skewness, changes in the

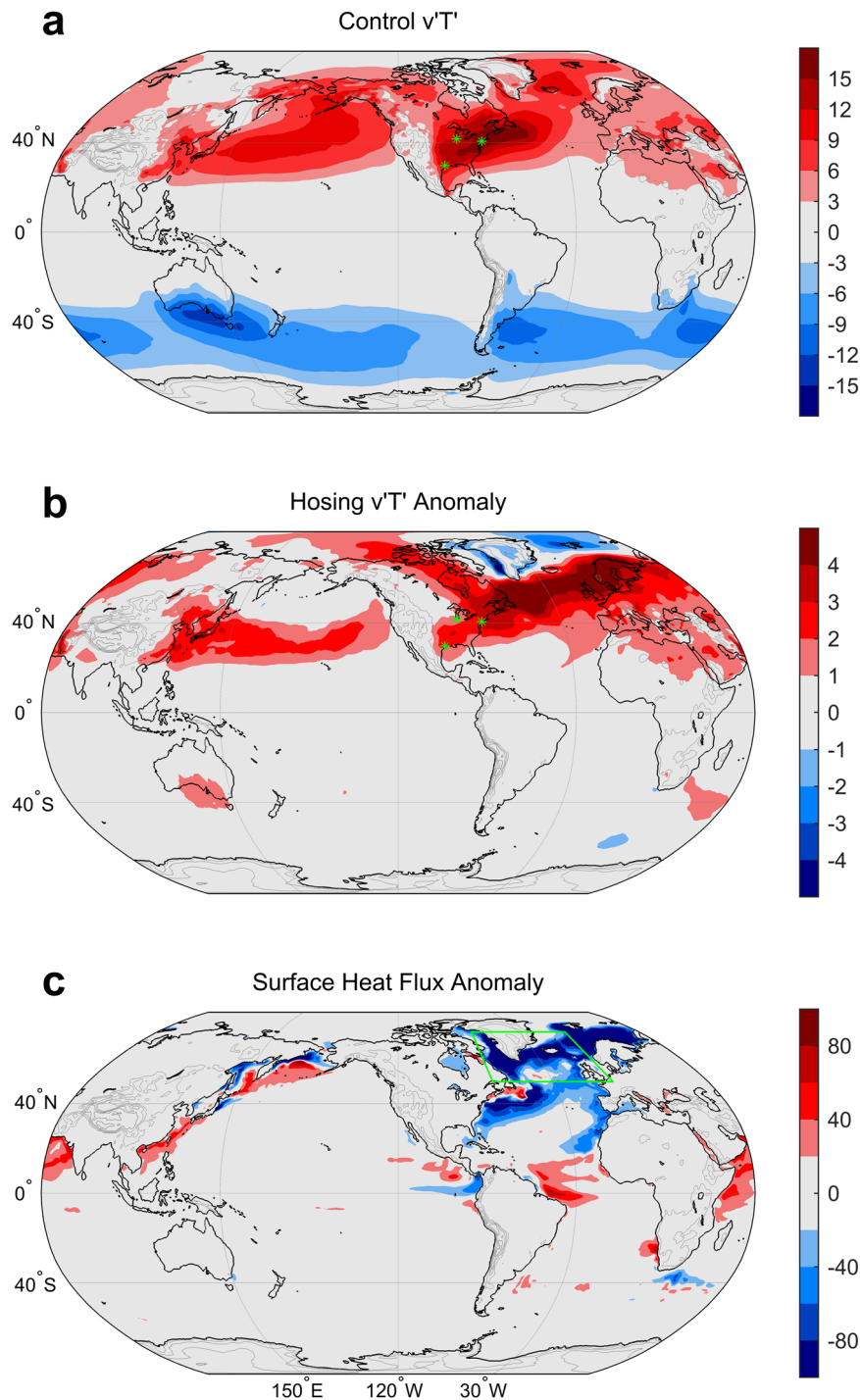


Fig. 2 Enhanced atmospheric heat transport by transient eddies in response to the shutdown of AMOC. **a** Atmospheric eddy temperature flux ($v'T'$) ($^{\circ}\text{C m s}^{-1}$) at 850 hPa in the long-term control. $v'T'$ is band passed using a Lanczos filter to identify synoptic variations on 3–15 days. Positive and negative values indicate northward and southward transport of sensible heat, respectively. The green asterisks mark Chicago, Houston, and New York. The thin grey lines are surface topography with 1000 m intervals. **b** Anomalies of the atmospheric eddy temperature flux ($^{\circ}\text{C m s}^{-1}$) during years 21–100 of the hosing experiment relative to the control. **c** Anomalies of the surface heat flux (W/m^2) during years 21–100 of the hosing experiment relative to the control. Negative values indicate reduction of the upward heat flux. The freshwater perturbation is input into the ocean region of the green box. All values in **a**, **b** and **c** are for DJF. See Supplementary Fig. 2 for the TOA and surface heat fluxes in the control run.

seasonal cycle (Supplementary Fig. 9), and individual extratropical cyclones/anti-cyclones that become stronger and propagate more southward. At New York, the mean cooling (-2.0°C), the increased standard deviation (from 4.7° to 5.4°C) and the reduced skewness (from 0.4 to 0), as well as more extreme individual weather events, all contribute to the drop of $\widehat{\Delta T}_s^{10}$ and $\widehat{\Delta T}_s^{100}$ in the hosing run

(Fig. 4e). Similarly, these factors are important to explain the intensification of extreme cold weather over western Europe (Fig. 5 and Supplementary Fig. 7), along with the increase in snow cover (Supplementary Fig. 10). However, snow cover in the hosing experiment changes little over the U.S. due to a minimum cooling (Fig. 5a).

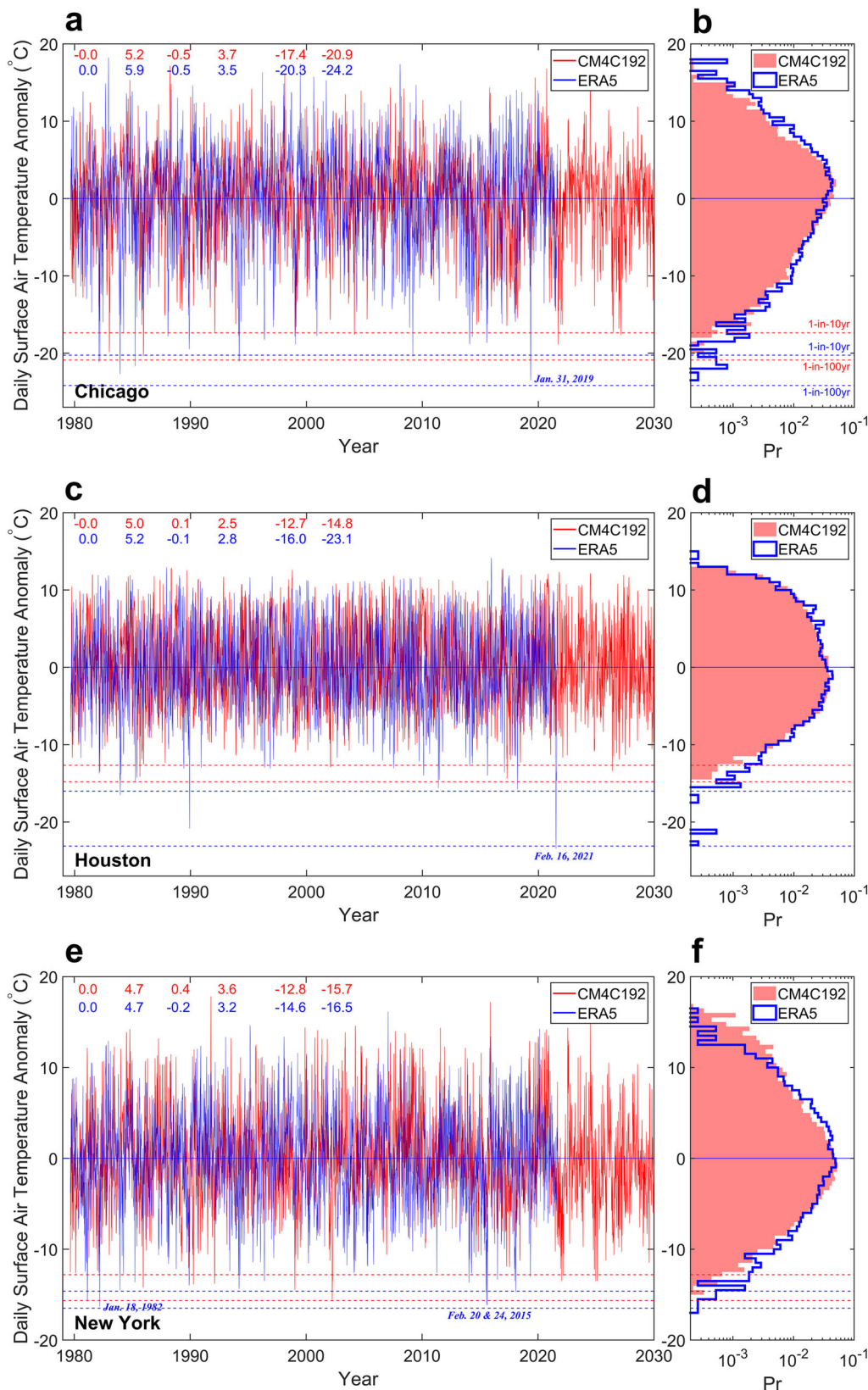


Fig. 3 Data-model comparison of DJF daily temperature anomalies (ΔT_s) at three cities of the U.S. a, b Chicago; c, d Houston; e, f New York. a, c, e The time series for 1979–2021 of ERA5 and the 50-year control simulation of CM4C192. Both curves are detrended and deseasonalized so that the mean is zero. The coldest value of ΔT_s at each city in ERA5 is marked with its occurrence date. **b, d, f** The histograms of the 42-year ERA5 data and the 100-year control simulation of CM4C192. Note that the x-axis uses a logarithmic scale and denotes probability (c_i/N ; c_i —bin count; N —total count). The solid horizontal lines show the mean. The dashed horizontal lines denote the return levels for the 1-in-10-year and 1-in-100-year cold events. Their values along with the mean and three moments of the time series are listed at the upper left corner. From left to right: mean, standard deviation, skewness, kurtosis, $\widehat{\Delta T_s}^{10}$, and $\widehat{\Delta T_s}^{100}$.

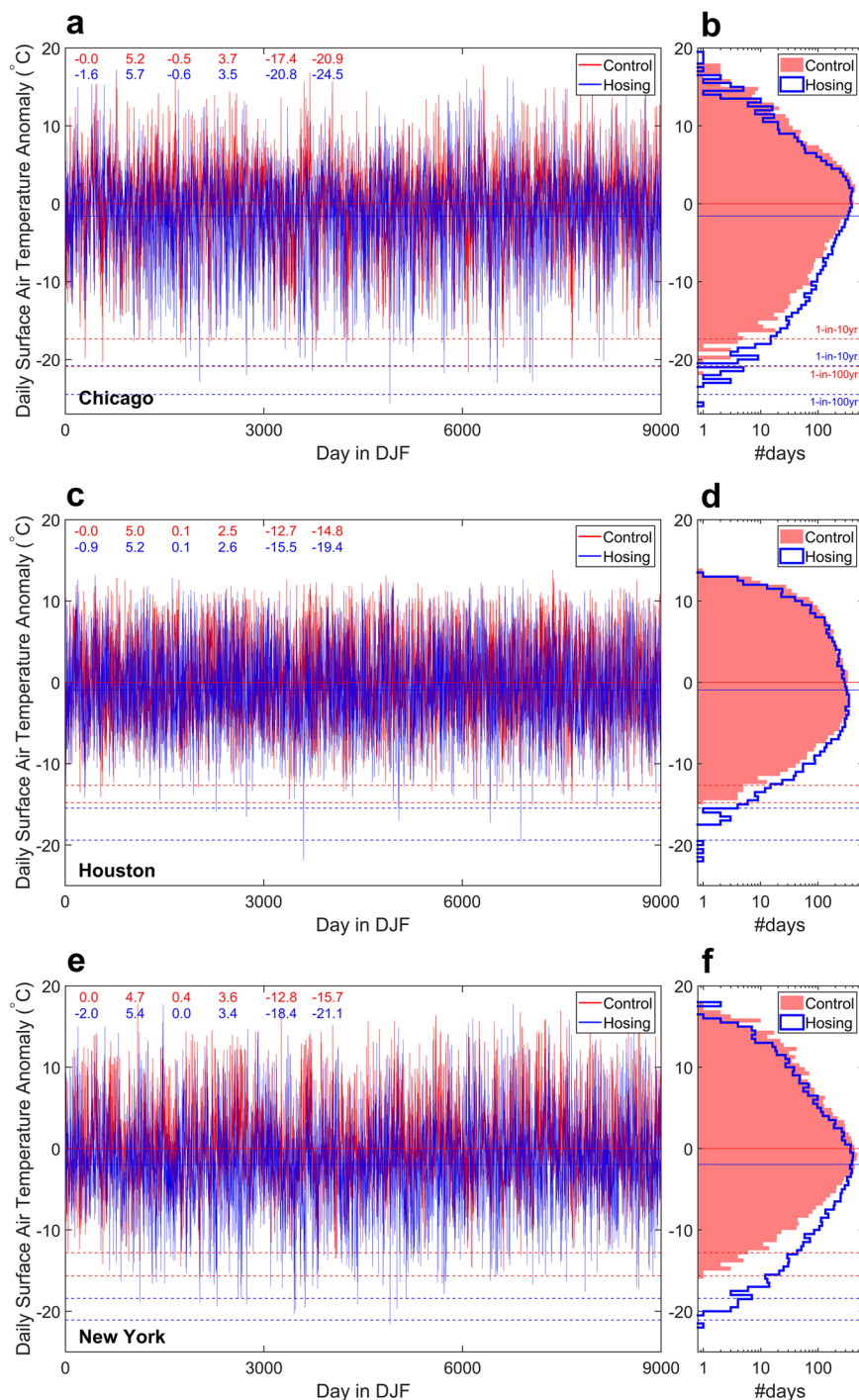


Fig. 4 Response of DJF daily temperature anomalies (ΔT_s) at three cities of the U.S. in the hosing experiment. **a, b** Chicago; **c, d** Houston; **e, f** New York. **a, c, e** Time series for 100 years or 9000 DJF days. In both curves, the daily climatology from the control has been removed and the mean cooling remains in the curve of the hosing run. **b, d, f** The histograms. The y-axis and x-axis are the temperature anomaly and the number of days, respectively. Note the x-axis uses a logarithmic scale. The solid horizontal lines show the long-term mean. The dashed horizontal lines denote the return levels for the 1-in-10-year and 1-in-100-year cold events. The statistics of the time series are listed at the upper left corner (from left to right: long-term mean, standard deviation, skewness, kurtosis, $\widehat{\Delta T_s}_{10}$ and $\widehat{\Delta T_s}_{100}$). These statistics are calculated based on years 1-100 of the control run and years 21-100 of the hosing run. The 90% confidence bounds of $\widehat{\Delta T_s}_{10}$ and $\widehat{\Delta T_s}_{100}$ quantified by the bootstrapping can be found in Supplementary Fig. 8.

By comparison, the drop of $\widehat{\Delta T_s}_{10}$ and $\widehat{\Delta T_s}_{100}$ at Houston is mainly caused by individual extreme weather events rather than by the overall variability and skewness (Fig. 4c). This is consistent with the increase in kurtosis that measures the tailedness of the temperature distribution (i.e., outliers). In fact, the large drops of $\widehat{\Delta T_s}_{100}$ in the Great Plains just east of the Rocky Mountains are

related to the increased kurtosis, which also dominates the ratio of the extreme and mean responses (Fig. 5d-f). The shutdown of AMOC sharpens the meridional temperature gradient at the northern mid-latitudes and increases the baroclinicity of the atmosphere. These lead to stronger weather systems that propagate more southward.

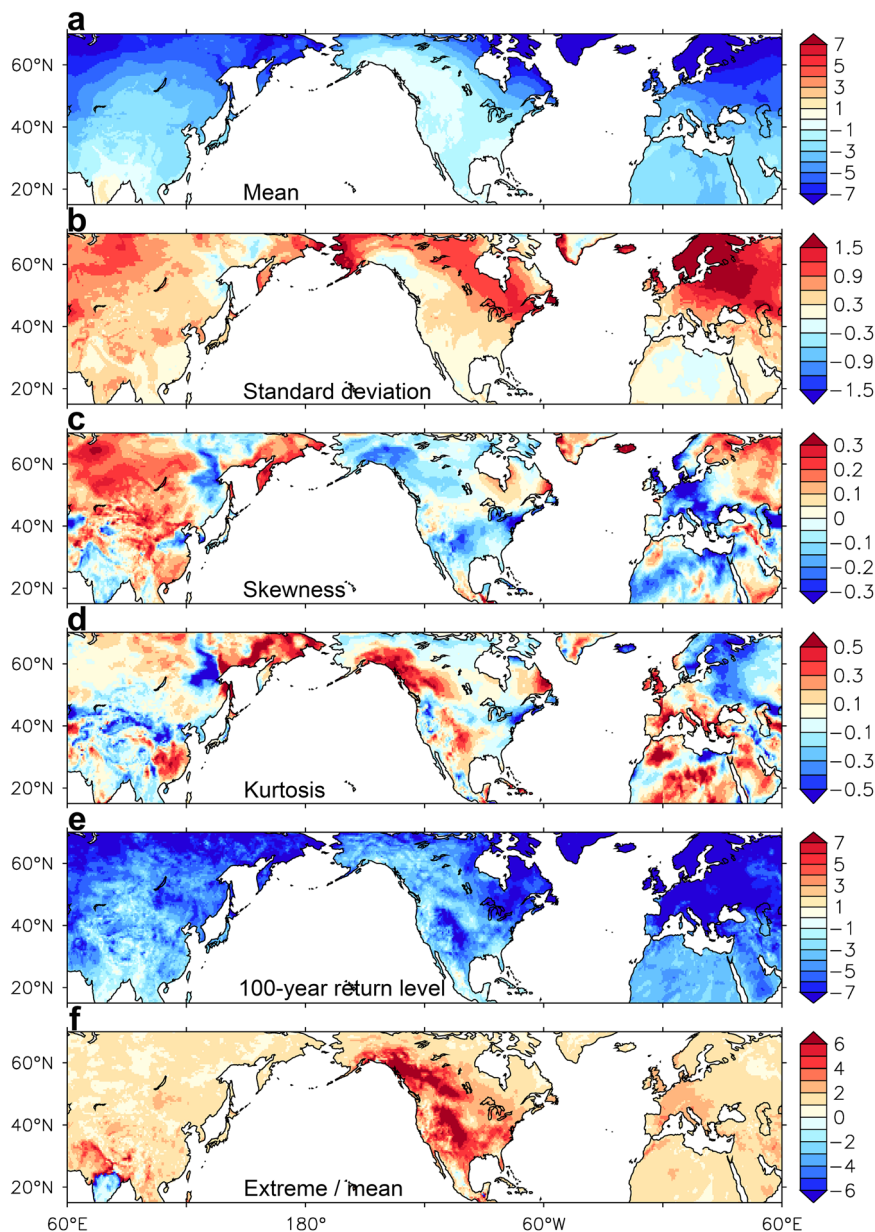


Fig. 5 Changes in statistics of DJF daily temperature anomalies (ΔT_s) over mid-latitude land areas in the hosing experiment. **a** Long-term mean ($^{\circ}\text{C}$), **b** Standard deviation ($^{\circ}\text{C}$), **c** Skewness, **d** Kurtosis, **e** 100-year return level (ΔT_s^{100} ; $^{\circ}\text{C}$); **f** Ratio of the extreme (**e**) and mean (**a**) responses. The values show the changes in statistics during years 21–100 of the hosing experiment relative to the long-term control. **f** Large positive values over North America indicate amplified responses of extremely cold daily temperature relative to the mean cooling. Negative values indicate that the extreme and mean temperature responses have opposite signs. See Supplementary Fig. 7 for these statistics in the long-term control simulation.

It should be noted that the analysis above is based on daily temperature anomalies (ΔT_s) relative to the daily climatology in the control (\tilde{T}_s). Due to the relatively small curvature of the seasonal cycle in DJF (Supplementary Fig. 9), the largest negative anomalies also mean the local coldest weather during winter. Among the three cities, Chicago is located in land interior and generally colder than the coastal Houston and New York. The absolute daily temperature (T_s) at Chicago could drop to as low as -27.4°C in the hosing run of CM4C192, compared with the coldest temperature of -14.3°C at Houston and -21.6°C at New York.

Conclusions

In this study, we use a state-of-the-art global weather/climate modeling system with high resolution to investigate the influence

of AMOC on extreme winter weather. Located at the upwind direction of the North Atlantic, mean winter temperatures over the U.S. are thought to be less influenced by the AMOC compared with the downwind European side (Fig. 5a and Supplementary Fig. 3b). From a concise energy balance point of view without involving much advanced atmospheric dynamics, we show here that AMOC can modulate daily temperature extremes more efficiently over the U.S. (Fig. 5e). The AMOC shutdown and reduced northward heat transport in the Atlantic are capable of exciting more extremely cold weather over the U.S. during winter. This amplified response at the tail of the temperature distribution could be several times larger than that of the mean (Fig. 5f).

This sensitivity of extreme weather over land interior to deep ocean circulation seems surprising but is nevertheless a robust response required by Bjerknes compensation. Due to the

north–south orientation of the mountain series over North America (Fig. 2), the Arctic outbreak during winter can push frigid polar air mass from Canada all the way southward to the Gulf of Mexico. We find that this channel of intense atmospheric heat exchange becomes even more active after the shutdown of AMOC, thereby intensifying extreme cold events over the U.S. In other words, an active AMOC in the present-day climate likely makes the U.S. winter less harsh and extreme.

According to some of recent observational studies, the AMOC has weakened during the past century⁴³. In particular, the northward heat transport at 26°N in the North Atlantic reduced by 0.17 PW and from 1.32 PW during 2004–2008 down to 1.15 PW during 2009–2016, as a result of a recent AMOC slowdown event³¹. This reduction in ocean heat transport influenced the northern atmosphere through heat flux anomalies at the ocean surface. The magnitude of this reduction represents a sizeable fraction of that induced by the AMOC shutdown in the CM4C192 simulations (Fig. 1).

Anyway, the model simulations carried out here represent a sensitivity study. Given the highly idealized nature of the hosing experiment in this study, one should be cautious about its implication for extreme cold weather in future climates. This is evidenced by the opposite trends of the mean temperature and Arctic sea ice between the ERA5 data and the CM4C192 simulation (Supplementary Fig. 3). Compared with the shutdown case, in addition, a slowdown of AMOC could cause a similar but more gradual response of the extreme weather. Despite these caveats, one sure thing is that Bjerknes compensation, which is derived from the very basic law of energy conservation, should continue to work in the future climate. Anything that alters one way of the energy flow will trigger a response from the others.

Methods

The GFDL CM4C192 model. CM4C192 is the high resolution version of the latest generation of the climate models developed and used at GFDL¹⁹. For various metrics, it performs among the best CMIP6 models⁴⁴. The atmospheric model (AM4)^{20–22} adopts finite-volume cubed-sphere dynamical core with 192 grid boxes per cube face (~0.5° grid spacing). It has 33 vertical levels and the model top is located at 1 hPa. The model incorporates updated physics such as a double-plume scheme for shallow and deep convection and a new mountain gravity wave drag parameterization²¹. Due to improvements in model resolution, physics and dynamics, CM4C192 simulates strong synoptic systems well such as hurricanes⁴⁵ and atmospheric rivers²².

The oceanic model of CM4C192 is based on the Modular Ocean Model version 6 (MOM6)²³. It uses the Arbitrary-Lagrangian-Eulerian algorithm in the vertical to allow for the combination of different vertical coordinates including geopotential and isopycnal. The model adopts the C-grid stencil in the horizontal and is configured on a tripolar grid. It has a 0.25° eddy-permitting horizontal resolution and 75 hybrid vertical layers down to the 6500 m maximum bottom depth. The vertical grid spacing can be as fine as 2 m near the ocean surface.

Daily or even hourly data of important atmospheric variables are saved to facilitate analyses on weather and extreme events. These variables include surface air temperature (T_s), precipitation, sea level pressure, atmospheric temperature (T) at 250 and 850 hPa, zonal and meridional winds (u , v) at 250 and 850 hPa, and specific humidity (q) at 850 hPa. The model uses a noleap calendar that has 365 days in every year.

Control run and water-hosing experiment with CM4C192. The initial condition is obtained from a long-term control simulation under the 1850 radiative forcing. During the 100-year control run under the 1950 radiative forcing, the global mean surface air temperature shows a slight increase (Supplementary Fig. 5a). This drift is mainly caused by some high-latitude regions. At low and mid-latitudes, T_s is quite stable in the control run without any clear trend (Supplementary Fig. 5b–d).

In the water-hosing experiment, a 0.6 Sv freshwater addition is input uniformly into the northern North Atlantic and the ocean region from 65°W–5°E and 50°N–75°N (see the green box in Fig. 2c) for 100 years. This freshwater addition is not compensated elsewhere. So it leads to about 5 m global sea level rise over the 100-year period. The perturbation freshwater is input at the same temperature as the local sea surface temperature. So while it is a mass source and reduces regional and global ocean salinity, it is not a specific heat source or sink and therefore does not influence the heat budget analysis here.

Atmospheric and Oceanic heat transport. In this study, we use both the direct and indirect methods to calculate the heat transport by the atmosphere and ocean. In the long-term control run, the total northward heat transport by the global atmosphere and global ocean at a latitude ϕ can be estimated by integrating the net radiative flux at TOA from the South (or North) Pole to latitude ϕ .

$$Q_i(\phi) = \int_{-\frac{\pi}{2}}^{\phi} \int_0^{2\pi} F_{\text{TOA}} R^2 \cos \phi' d\lambda d\phi' \quad (1)$$

Q_i is the total northward heat transport; F_{TOA} the net radiative flux at TOA; R Earth's radius; λ and ϕ are longitude and latitude, respectively. Similarly, the atmospheric heat transport (Q_a) is estimated as

$$Q_a(\phi) = \int_{-\frac{\pi}{2}}^{\phi} \int_0^{2\pi} (F_{\text{TOA}} - F_{\text{sfic}}) R^2 \cos \phi' d\lambda d\phi', \quad (2)$$

where F_{sfic} is the heat flux at the surface.

We adopt the direct method to calculate the heat transport in an ocean basin. Integrate the transport from the western to the eastern boundary and vertically. Then sum across the ocean basins.

$$Q_o(\phi) = \sum_{\text{basin}} \int_{-H}^{\eta} \int_w^e \rho_w c_p T v R \cos \phi d\lambda dz \quad (3)$$

Q_o is the global ocean heat transport, T the ocean potential temperature, v the ocean meridional velocity, ρ_w seawater density, c_p seawater heat capacity, η and H denote ocean surface and bottom, respectively.

Sensible and latent heat fluxes from the atmospheric transient Eddies. To calculate the atmospheric eddy heat fluxes, we apply a Lanczos bandpass filter⁴⁶ to daily atmospheric temperature (T), specific humidity (q), and meridional wind (v) to identify their variations on the synoptic timescale of 3–15 days. We first remove the seasonal cycle before applying the filter to the time series.

$$x'(t) = \sum_{k=-L}^L w(k)x(t-k) \quad (4)$$

$$w(k) = \left(\frac{\sin 2\pi f_2 k}{\pi k} - \frac{\sin 2\pi f_1 k}{\pi k} \right) \frac{\sin \pi k / L}{\pi k / L} \quad (5)$$

$$k = -L, \dots, 0, \dots, L$$

x and x' represent the original and filtered time series of T , q or v , respectively. f_1 and f_2 are the cutoff frequencies for the bandpass filter. $w(k)$ represents a set of weights within the filter window ($L = 25$).

Analysis on extreme daily surface air temperature. The anomaly of daily surface air temperature is the departure from its daily climatology.

$$\Delta T_s(x, y, t) = T_s(x, y, t) - \bar{T}_s(x, y, t_1), t_1 = 1, 2, \dots, 365 \quad (6)$$

T_s , \bar{T}_s and ΔT_s are daily temperature, its climatology and anomaly, respectively. As the coldest three months at the mid-latitude Northern Hemisphere, \bar{T}_s over DJF shows relatively small variation compared with the annual cycle (Supplementary Fig. 9). Note that ΔT_s in the hosing experiment is calculated relative to \bar{T}_s in the control. So the change in the seasonal cycle (mean, amplitude and timing) in the hosing run also contributes to ΔT_s (Supplementary Fig. 9).

To calculate return levels of extremely cold daily temperatures, we use the block maxima approach in the extreme value analysis^{41,47}. We consider the time series of $-\Delta T_s$ and pick out the maximum daily values (i.e., the coldest daily temperatures) in DJF for each year. Then we fit the generalized extreme value (GEV) distribution to annual maxima of $-\Delta T_s$.

$$G(x) = \exp\left\{-\left[1 + k\left(\frac{x-\mu}{\sigma}\right)^{-\frac{1}{k}}\right]\right\} \quad (7)$$

$$1 + k\frac{x-\mu}{\sigma} > 0$$

k , σ , and μ are the shape, scale and location parameters of GEV, respectively. For $k = 0$, the GEV distribution reduces to the Gumbel distribution. For $k > 0$ and $k < 0$, the GEV distribution becomes the Fréchet and Weibull distribution, respectively. After the three parameters are determined, the return levels ($\widehat{\Delta T}_s^{10}$ and $\widehat{\Delta T}_s^{100}$) can be estimated with the inverse cumulative density function of the GEV distribution. For example,

$$-\widehat{\Delta T}_s^{100} = \mu - \frac{\sigma}{k} \left\{ 1 - \left[-\ln\left(1 - \frac{1}{100}\right) \right]^{-k} \right\} \quad (8)$$

To assess the uncertainty associated with the return level estimates and determine whether the changes in return level in the hosing experiment are statistically significant, we use the bootstrap method^{41,48} to generate 10,000 samples of the annual maximum values of $-\Delta T_s$ and quantify the 90% confidence bounds.

ERA5 reanalysis. ERA5 combines large amounts of historical observations and uses advanced modeling and data assimilation to obtain global estimates of the atmosphere⁴⁰. For the data-model comparison in this study, we use the 3-h global surface air temperature data from January 1, 1979 to February 28, 2021. The data with a 0.25° horizontal resolution are downloaded from the Copernicus Climate Change Service (<https://doi.org/10.24381/cds.adbb2d47>). February 29 in the leap years is removed before the data-model comparison.

Data availability

The control simulation of GFDL CM4C192 can be found at the CMIP6 archive (<https://esgf-node.llnl.gov/projects/cmip6/>). ERA5 reanalysis data can be found at <https://climate.copernicus.eu/climate-reanalysis>. Supplementary Data 1–3 contain data that were used to generate Figs. 1, 3, and 4.

Code availability

The model codes can be found at <https://www.gfdl.noaa.gov/coupled-physical-model-cm4/>. All other codes used in the analysis of this study are available from the corresponding author upon request.

Received: 5 May 2021; Accepted: 23 September 2021;

Published online: 13 October 2021

References

- Stouffer, R. J. et al. Investigating the causes of the response of the thermohaline circulation to past and future climate changes. *J. Clim.* **19**, 1365–1387 (2006).
- Manabe, S. & Stouffer, R. J. The role of thermohaline circulation in climate. *Tellus B* **51**, 91–109 (1999).
- Zhang, R. & Delworth, T. L. Simulated tropical response to a substantial weakening of the Atlantic thermohaline circulation. *J. Clim.* **18**, 1853–1860 (2005).
- Gregory, J. M. et al. A model intercomparison of changes in the Atlantic thermohaline circulation in response to increasing atmospheric CO₂ concentration. *Geophys. Res. Lett.* **32**, L12703 (2005).
- Vellinga, M. & Wood, R. A. Global climatic impacts of a collapse of the Atlantic thermohaline circulation. *Clim. Change* **54**, 251–267 (2002).
- Rahmstorf, S. & Ganopolski, A. Long-term global warming scenarios computed with an efficient coupled climate model. *Clim. Change* **43**, 353–367 (1999).
- Levermann, A., Griesel, A., Hofmann, M., Montoya, M. & Rahmstorf, S. Dynamic sea level changes following changes in the thermohaline circulation. *Clim. Dyn.* **24**, 347–354 (2005).
- Yin, J., Schlesinger, M. E. & Stouffer, R. J. Model projections of rapid sea-level rise on the northeast coast of the United States. *Nat. Geosci.* **2**, 262–266 (2009).
- Jackson, L. et al. Global and European climate impacts of a slowdown of the AMOC in a high resolution GCM. *Clim. Dyn.* **45**, 3299–3316 (2015).
- Sigmond, M., Fyfe, J. C., Saenko, O. A. & Swart, N. C. Ongoing AMOC and related sea-level and temperature changes after achieving the Paris targets. *Nat. Clim. Change* **10**, 672–677 (2020).
- Liu, W., Fedorov, A. V., Xie, S.-P. & Hu, S. Climate impacts of a weakened Atlantic Meridional overturning circulation in a warming climate. *Sci. Adv.* **6**, eaaz4876 (2020).
- Yin, J., Griffies, S. M., Winton, M., Zhao, M. & Zanna, L. Response of storm-related extreme sea level along the US Atlantic coast to combined weather and climate forcing. *J. Clim.* **33**, 3745–3769 (2020).
- Duchez, A. et al. Drivers of exceptionally cold North Atlantic Ocean temperatures and their link to the 2015 European heat wave. *Environ. Res. Lett.* **11**, 074004 (2016).
- Schenk, F. et al. Warm summers during the Younger Dryas cold reversal. *Nat. Commun.* **9**, 1–13 (2018).
- Rousi, E., Seltner, F., Rahmstorf, S. & Coumou, D. Changes in North Atlantic atmospheric circulation in a warmer climate favor winter flooding and summer drought over Europe. *J. Clim.* **34**, 2277–2295 (2021).
- Bryden, H. L., King, B. A., McCarthy, G. D. & McDonagh, E. L. Impact of a 30% reduction in Atlantic meridional overturning during 2009–2010. *Ocean Sci.* **10**, 683–691 (2014).
- Hallam, S. et al. Ocean precursors to the extreme Atlantic 2017 hurricane season. *Nat. Commun.* **10**, 1–10 (2019).
- Woollings, T., Gregory, J. M., Pinto, J. G., Reyers, M. & Brayshaw, D. J. Response of the North Atlantic storm track to climate change shaped by ocean–atmosphere coupling. *Nat. Geosci.* **5**, 313–317 (2012).
- Held, I. M. et al. Structure and performance of GFDL’s CM4.0 climate model. *J. Adv. Model. Earth Syst.* **11**, 3691–3727 (2019).
- Zhao, M. et al. The GFDL global atmosphere and land model AM4.0/LM4.0: 1. Simulation characteristics with prescribed SSTs. *J. Adv. Model. Earth Syst.* **10**, 691–734 (2018).
- Zhao, M. et al. The GFDL global atmosphere and land model AM4.0/LM4.0: 2. Model description, sensitivity studies, and tuning strategies. *J. Adv. Model. Earth Syst.* **10**, 735–769 (2018).
- Zhao, M. Simulations of atmospheric rivers, their variability, and response to global warming using GFDL’s new high-resolution general circulation model. *J. Clim.* **33**, 10287–10303 (2020).
- Adcroft, A. et al. The GFDL global ocean and sea ice model OM4.0: model description and simulation features. *J. Adv. Model. Earth Syst.* **11**, 3167–3271 (2019).
- Doss-Gollin, J., Farnham, D. J., Lall, U. & Modi, V. How unprecedented was the February 2021 Texas cold snap? *Environ. Res. Lett.* **16**, 064056 (2021).
- Busby, J. W. et al. Cascading risks: understanding the 2021 winter blackout in Texas. *Energy Res. Soc. Sci.* **77**, 102106 (2021).
- Haarsma, R. J. et al. High resolution model intercomparison project (HighResMIP v1. 0) for CMIP6. *Geosci. Model Dev.* **9**, 4185–4208 (2016).
- Peixoto, J. P. & Oort, A. H. *Physics of Climate* (Springer, 1992).
- Trenberth, K. E. & Caron, J. M. Estimates of meridional atmosphere and ocean heat transports. *J. Clim.* **14**, 3433–3443 (2001).
- Fasullo, J. T. & Trenberth, K. E. The annual cycle of the energy budget. Part II: Meridional structures and poleward transports. *J. Clim.* **21**, 2313–2325 (2008).
- Johns, W. E. et al. Continuous, array-based estimates of Atlantic Ocean heat transport at 26.5N. *J. Clim.* **24**, 2429–2449 (2011).
- Bryden, H. L. et al. Reduction in ocean heat transport at 26N since 2008 cools the eastern subpolar gyre of the North Atlantic Ocean. *J. Clim.* **33**, 1677–1689 (2020).
- Bjerknes, J. *Advances in Geophysics* Vol. 10, 1–82 (Elsevier, 1964).
- Shaffrey, L. & Sutton, R. Bjerknes compensation and the decadal variability of the energy transports in a coupled climate model. *J. Clim.* **19**, 1167–1181 (2006).
- Zhang, R. & Delworth, T. L. Impact of the Atlantic multidecadal oscillation on North Pacific climate variability. *Geophys. Res. Lett.* **34**, 23 (2007).
- Yang, H. et al. Heat transport compensation in atmosphere and ocean over the past 22,000 years. *Sci. Rep.* **5**, 1–11 (2015).
- Otten, S., Esau, I. & Ottera, O. H. Bjerknes compensation in the CMIP5 climate models. *J. Clim.* **31**, 8745–8760 (2018).
- Lutsko, N. J., Baldwin, J. W. & Cronin, T. W. The impact of large-scale orography on Northern Hemisphere winter synoptic temperature variability. *J. Clim.* **32**, 5799–5814 (2019).
- Winton, M. On the climatic impact of ocean circulation. *J. Clim.* **16**, 2875–2889 (2003).
- Herweijer, C., Seager, R., Winton, M. & Clement, A. Why ocean heat transport warms the global mean climate. *Tellus A* **57**, 662–675 (2005).
- Hersbach, H. et al. The ERA5 global reanalysis. *QJRM* **146**, 1999–2049 (2020).
- Zwiers, F. W. & Kharin, V. V. Changes in the extremes of the climate simulated by CCC GCM2 under CO₂ doubling. *J. Clim.* **11**, 2200–2222 (1998).
- McKinnon, K. A., Rhines, A., Tingley, M. P. & Huybers, P. The changing shape of Northern Hemisphere summer temperature distributions. *J. Geophys. Res.* **121**, 8849–8868 (2016).
- Caesar, L., McCarthy, G., Thornalley, D., Cahill, N. & Rahmstorf, S. Current Atlantic Meridional overturning circulation weakest in last millennium. *Nat. Geosci.* **11**, 1–3 (2021).
- Boucher, O. et al. Presentation and evaluation of the IPSL-CM6A-LR climate model. *J. Adv. Model. Earth Syst.* **12**, e2019MS002010 (2020).
- Murakami, H. et al. Detected climatic change in global distribution of tropical cyclones. *Proc. Natl Acad. Sci. USA* **117**, 10706–10714 (2020).
- Duchon, C. E. Lanczos filtering in one and two dimensions. *J. Appl. Meteorol. Climatol.* **18**, 1016–1022 (1979).
- Coles, S., Bawa, J., Trenner, L. & Dorazio, P. *An Introduction to Statistical Modeling of Extreme Values* (Springer, 2001).
- Efron, B. *The Jackknife, the Bootstrap and other Resampling Plans* (SIAM, 1982).

Acknowledgements

We thank Ron Stouffer, Zhihong Tan, and two reviewers for their comments, and ECMWF and the Copernicus Climate Change Service for providing the ERA5 reanalysis data. The work is supported by the NOAA Climate Program Office (Grant # NA18OAR4310267).

Author contributions

J.Y. initiated the idea and M.Z. carried out the CM4C192 simulations. J.Y. led the data analysis and manuscript writing. Both discussed the results and contributed to the improvement of the manuscript.

Competing interests

The authors declare no competing interests.

Additional information

Supplementary information The online version contains supplementary material available at <https://doi.org/10.1038/s43247-021-00290-9>.

Correspondence and requests for materials should be addressed to Jianjun Yin.

Peer review information *Communications Earth & Environment* thanks Fuyao Wang and the other, anonymous, reviewer(s) for their contribution to the peer review of this work. Primary Handling Editor: Heike Langenberg.

Reprints and permission information is available at <http://www.nature.com/reprints>

Publisher's note Springer Nature remains neutral with regard to jurisdictional claims in published maps and institutional affiliations.



Open Access This article is licensed under a Creative Commons Attribution 4.0 International License, which permits use, sharing, adaptation, distribution and reproduction in any medium or format, as long as you give appropriate credit to the original author(s) and the source, provide a link to the Creative Commons license, and indicate if changes were made. The images or other third party material in this article are included in the article's Creative Commons license, unless indicated otherwise in a credit line to the material. If material is not included in the article's Creative Commons license and your intended use is not permitted by statutory regulation or exceeds the permitted use, you will need to obtain permission directly from the copyright holder. To view a copy of this license, visit <http://creativecommons.org/licenses/by/4.0/>.

© The Author(s) 2021